ELSEVIER

International Journal of Solids and Structures 41 (2004) 827–845

INTERNATIONAL JOURNAL OF
SOLIDS and
STRUCTURES

www.elsevier.com/locate/ijsolstr

Notch-sensitive fracture of polycarbonate

B.P. Gearing, L. Anand *

Department of Mechanical Engineering, Massachusetts Institute of Technology, Room 1-310, 77 Mass. Ave.,
MIT, Cambridge, MA 02139, USA

Received 22 May 2003; received in revised form 10 September 2003

Abstract

We have developed a constitutive model and fracture criteria which can capture the competition between the ductile mechanism of inelastic deformation by "shear-yielding" and eventual ductile tearing, typically observed in polycarbonate under states of low triaxial tension, and the brittle cracking phenomenon that is observed in states of high triaxial tension. We have implemented the constitutive model in a finite element computer program which permits the modelling of failure, when user-specified fracture criteria are met, by an element removal technique. We show that our theory, when suitably implemented and calibrated, is able to *quantitatively* predict the experimentally-observed ductile failure response of blunt-notched beams, as well as the competition between the brittle and ductile mechanisms in more sharply-notched beams of polycarbonate in bending.

Keywords: Polymeric material; Constitutive behavior; Fracture criteria; Mechanical testing; Finite elements

---

1. Introduction

Engineering thermoplastics such as polycarbonate which exhibit significant ductility, as evidenced by large strains to failure in smooth-bar tension or compression experiments, have been found to be significantly notch-sensitive, in that they exhibit a brittle mode of failure in notched specimens which generate a state of sufficiently large hydrostatic tension ahead of the notch (e.g. Ishikawa et al., 1977; Zuber, 1985; Nimmer and Woods, 1992; Narisawa and Yee, 1993). Experimental observations on notched specimens of polycarbonate tested in monotonic bending at moderately slow rates at room temperature show that (a) if the notch has a reasonably large root radius, then failure is initiated by ductile tearing at the notch root, while (b) if the notch has a relatively small root radius, then the failure initiates in the form of a crack-like feature *at the tip of the plastic zone surrounding the notch*, in the region of high hydrostatic tension (e.g., see Fig. 6 of Ishikawa et al., 1977; also see Figs. 15-5 and 15-61 of Narisawa and Yee, 1993). These crack-like features have been called *internal crazes* by Narisawa and his colleagues (e.g. Ishikawa et al., 1977;

---

[*] Corresponding author. Tel.: +1-617-253-1635; fax: +1-617-258-8742.
E-mail address: anand@mit.edu (L. Anand).

0020-7683/$ - see front matter © 2003 Elsevier Ltd. All rights reserved.
doi:10.1016/j.ijsolstr.2003.09.058

Narisawa and Yee, 1993).[1] However, it is unclear whether the internal crack-like features observed at sharp notch-roots in polycarbonate exhibit the characteristic microstructural morphology in which the faces of the crack-like features are bridged by highly-oriented fibrils, as is typical for crazes in polymeric materials. Accordingly, here we refrain from calling these internal crack-like features crazes, and simply associate the initiation of such features at sharp notch-roots to be the outcome of internal cavitation in the material.

Many experiments indicate that a hydrostatic tension plays a key role in the nucleation of such an internal crack, and a critical value of the hydrostatic tension, σ_c, has been suggested as a suitable criterion for the nucleation of internal cracks (e.g. Ishikawa et al., 1977; Nimmer and Woods, 1992). For example, Narisawa and his colleagues have estimated σ_c for slow-cooled polycarbonate to be approximately 87–89 MPa; to obtain such an estimated they used classical slip-line field analysis, coupled with a measurement of the craze location below the notch-tip in three-point bending experiments.[2] A similar estimate of $\sigma_c \approx 90$–100 MPa for polycarbonate has been obtained by Nimmer and Woods (1992); they performed a finite element analysis, using a non-hardening J_2-flow theory of plasticity, of a three-point bending experiment to determine the hydrostatic stress field at the instant when the corresponding physical experiment showed a load drop due to the initiation of an internal crack.

The purpose of this brief paper is to develop a constitutive model and failure criteria which can capture the competition between the ductile mechanism of inelastic deformation by "shear-yielding" and the eventual ductile tearing, typically observed in amorphous thermoplastic materials under states of low triaxial tension, and the brittle internal cracking phenomenon that is observed in states of high triaxial tension. A significant advance in modelling the plastic deformation of amorphous polymers by shear-yielding has been made by Parks and their co-workers (e.g. Parks et al., 1985; Boyce et al., 1988; Arruda and Boyce, 1993), and Wu and Van der Giessen (1993). More recently, Anand and Gurtin (2004) have reformulated the theory within a rigorous thermodynamic framework, and introduced an internal-state variable in the theory to represent the local free-volume in the material to capture the highly non-linear stress–strain behavior that precedes the yield-peak and gives rise to post-yield strain-softening. We shall build on this model for plastic deformation of glassy polymers developed by the aforementioned authors. In particular, we shall extend the model to *allow for large local elastic volumetric changes*, and as a first attempt to model fracture in such materials we will introduce two simple local fracture criteria: (a) Brittle fracture will be taken to have occurred when a local elastic volumetric strain has reached a critical value. (b) Ductile fracture will be taken to have occurred when a local measure of plastic deformation, *an effective plastic stretch*, has reached a critical value. We shall show that the constitutive model and failure criteria, when suitably calibrated, are able to *quantitatively* predict the ductile failure response of blunt-notched beams, as well as the competition between the ductile and brittle mechanisms in more sharply-notched beams of polycarbonate in bending.

The plan of this paper is as follows. In Section 2 we summarize our constitutive model and fracture criteria. In Section 3 we describe our experiments to calibrate the material parameters in the model. In Section 4 we compare our numerical predictions for both the deformation and failure response of a

---

[1] They use this terminology to distinguish the internal crazes from *surface crazes*. Surface crazing is a complex phenomenon which is time and temperature-dependent, and the initiation of surface crazes is strongly affected by the environment, especially the presence of organic liquids. In contrast, the occurrence of internal crazes is due primarily to mechanical conditions, and the environment plays little or no role in their initiation and growth. However, unlike surface crazes which exhibit a microstructural morphology in which the craze faces are bridged by highly-oriented fibrils (c.f., Fig. 15-6 of Narisawa and Yee, 1993), post-mortem examination of the faces of the crack-like features of internal crazes observed in polycarbonate shows them to be relatively smooth and featureless, similar to cleavage facets in metallic materials (Zuber, 1985).

[2] Estimates of σ_c for initiation of internal cracks in other amorphous glassy polymers are given in Table 15-1 of Narisawa and Yee (1993).

"blunt"-notched specimen geometry and a "sharp"-notched specimen geometry of polycarbonate under four-point bending. We close in Section 5 with some final remarks.

2. Constitutive equations for plastic deformation. Fracture criteria

In this section we begin by summarizing the constitutive model of Anand and Gurtin (2004) for plastic deformation of amorphous polymeric materials. We consider an isothermal theory in the absence of temperature gradients based on the multiplicative decomposition, $\mathbf{F} = \mathbf{F}^{\mathrm{e}}\mathbf{F}^{\mathrm{p}}$, of the deformation gradient $\mathbf{F}$ into elastic and plastic parts, $\mathbf{F}^{\mathrm{e}}$ and $\mathbf{F}^{\mathrm{p}}$ (Kroner, 1960; Lee, 1969). [3] The theory also contains two internal variables: a variable $s > 0$ that represents an isotropic intermolecular resistance to plastic flow; and an unsigned variable η that represents the local change in free-volume. [4] Then, in terms of the variables

ψ,	Helmholtz free energy per unit volume of the relaxed configuration,
$\mathbf{T}$, $\mathbf{T} = \mathbf{T}^{\mathrm{T}}$,	Cauchy stress,
$\mathbf{F}$, $\det \mathbf{F} > 0$,	deformation gradient,
$\mathbf{F}^{\mathrm{p}}$, $\det \mathbf{F}^{\mathrm{p}} = 1$,	plastic part of the deformation gradient,
s, $s > 0$,	isotropic resistance to plastic flow,
η,	change in free-volume,

and the definitions

$\mathbf{F}^{\mathrm{e}} = \mathbf{F}\mathbf{F}^{\mathrm{p}-1}$, $\det\mathbf{F}^{\mathrm{e}} > 0$,	elastic deformation gradient,
$\mathbf{C}^{\mathrm{e}} = \mathbf{F}^{\mathrm{e}^{\mathrm{T}}}\mathbf{F}^{\mathrm{e}}$,	elastic right Cauchy–Green strain,
$\mathbf{E}^{\mathrm{e}} = \frac{1}{2}(\mathbf{C}^{\mathrm{e}} - \mathbf{1})$,	elastic strain,
$\mathbf{T}^{\mathrm{e}} = \mathbf{R}^{\mathrm{eT}}\mathbf{T}\mathbf{R}^{\mathrm{e}}$,	stress conjugate to the elastic strain $\mathbf{E}^{\mathrm{e}}$,
$\sigma = \frac{1}{3}\operatorname{tr}\mathbf{T}$,	mean normal stress,
$\mathbf{T}^{\mathrm{e}}_0 = \mathbf{T}^{\mathrm{e}} - \sigma\mathbf{1}$,	deviatoric stress,
$\mathbf{B}^{\mathrm{p}} = \mathbf{F}^{\mathrm{p}}\mathbf{F}^{\mathrm{pT}}$,	left Cauchy–Green tensor corresponding to $\mathbf{F}^{\mathrm{p}}$,
$\mathbf{B}^{\mathrm{p}}_0 = \mathbf{B}^{\mathrm{p}} - \frac{1}{3}(\operatorname{tr}\mathbf{B}^{\mathrm{p}})\mathbf{1}$,	deviatoric part of $\mathbf{B}^{\mathrm{p}}$,
$\lambda^{\mathrm{p}} = \frac{1}{\sqrt{3}}\sqrt{\operatorname{tr}\mathbf{B}^{\mathrm{p}}}$,	effective plastic stretch,
$\mathbf{D}^{\mathrm{p}} = \operatorname{sym}(\dot{\mathbf{F}}^{\mathrm{p}}\mathbf{F}^{\mathrm{p}-1}), \operatorname{tr}\mathbf{D}^{\mathrm{p}} = 0$,	plastic stretching,

the constitutive equations, *under the approximative assumption of small elastic stretches*, are:

(1) *Free energy*:

The Helmholtz free energy is taken in the non-interactive form

$$\psi = \psi^{\mathrm{e}}(\mathbf{E}^{\mathrm{e}}) + \psi^{\mathrm{p}}(\lambda^{\mathrm{p}}), \tag{2.1}$$

---

[3] *Notation*: ∇ and Div denote the gradient and divergence with respect to the material point $\mathbf{X}$ in the *reference configuration*; grad and div denote these operators with respect to the point $\mathbf{x} = \mathbf{y}(\mathbf{X}, t)$ in the deformed configuration, where $\mathbf{y}(\mathbf{X}, t)$ is the motion; a superposed dot denotes the material time-derivative. Throughout, we write $\mathbf{F}^{\mathrm{e}-1} = (\mathbf{F}^{\mathrm{e}})^{-1}$, $\mathbf{F}^{\mathrm{p}-\mathrm{T}} = (\mathbf{F}^{\mathrm{p}})^{-\mathrm{T}}$, etc. We write sym $\mathbf{A}$, skw $\mathbf{A}$, respectively, for the symmetric, and skew parts of a tensor $\mathbf{A}$. Also, the inner product of tensors $\mathbf{A}$ and $\mathbf{B}$ is denoted by $\mathbf{A} \cdot \mathbf{B}$, and the magnitude of $\mathbf{A}$ by $|\mathbf{A}| = \sqrt{\mathbf{A} \cdot \mathbf{A}}$.

[4] It is commonly believed that the evolution of the local free-volume is the major reason for the highly non-linear stress–strain behavior of glassy materials, which precedes the yield-peak and gives rise to the post-yield strain-softening.

where ψ^{e} is an elastic free energy, and ψ^{p} a plastic free energy. The elastic free energy is taken in the standard form for small elastic stretches

$$\psi^{\mathrm{e}} = G|\mathbf{E}_0^{\mathrm{e}}|^2 + \frac{1}{2}K|\mathrm{tr}\,\mathbf{E}^{\mathrm{e}}|^2, \tag{2.2}$$

where G and K are the elastic shear and bulk moduli, respectively. In amorphous polymeric materials the major part of ψ^{p} arises from an "entropic" contribution, and motivated by statistical mechanics models of rubber elasticity, [5] is taken in the specific form

$$\psi^{\mathrm{p}} = \mu_{\mathrm{R}}\lambda_{\mathrm{L}}^2\left[\left(\frac{\lambda^{\mathrm{p}}}{\lambda_{\mathrm{L}}}\right)x + \ln\left(\frac{x}{\sinh x}\right) - \left(\frac{1}{\lambda_{\mathrm{L}}}\right)y - \ln\left(\frac{y}{\sinh y}\right)\right], \tag{2.3}$$

$$x = \mathscr{L}^{-1}\left(\frac{\lambda^{\mathrm{p}}}{\lambda_{\mathrm{L}}}\right), \quad y = \mathscr{L}^{-1}\left(\frac{1}{\lambda_{\mathrm{L}}}\right), \tag{2.4}$$

where $\mathscr{L}^{-1}$ is the inverse [6] of the Langevin function $\mathscr{L}(\cdots) = \coth(\cdots) - (\cdots)^{-1}$. This functional form for ψ^{p} involves two material parameters: μ_{R}, called the rubbery modulus, and λ_{L}, called the network locking stretch.

(2) *Equation for the stress*:

$$\mathbf{T}^{\mathrm{e}} = \frac{\partial\psi^{\mathrm{e}}}{\partial\mathbf{E}^{\mathrm{e}}} = 2G\mathbf{E}_0^{\mathrm{e}} + K(\mathrm{tr}\,\mathbf{E}^{\mathrm{e}})\mathbf{1}. \tag{2.5}$$

(3) *Equation for back stress*: [7]

$$\mathbf{S}_{\mathrm{back}} = 2\mathrm{sym}_0\left(\frac{\partial\psi^{\mathrm{p}}}{\partial\mathbf{B}^{\mathrm{p}}}\mathbf{B}^{\mathrm{p}}\right) = \mu\mathbf{B}_0^{\mathrm{p}}, \tag{2.6}$$

with

$$\mu = \frac{1}{3\lambda^{\mathrm{p}}}\frac{\partial\psi^{\mathrm{p}}}{\partial\lambda^{\mathrm{p}}} = \mu_{\mathrm{R}}\left(\frac{\lambda_{\mathrm{L}}}{3\lambda^{\mathrm{p}}}\right)\mathscr{L}^{-1}\left(\frac{\lambda^{\mathrm{p}}}{\lambda_{\mathrm{L}}}\right). \tag{2.7}$$

The back stress modulus $\mu \to \infty$ as $\lambda^{\mathrm{p}} \to \lambda_{\mathrm{L}}$, since $\mathscr{L}^{-1}(z) \to \infty$ as $z \to 1$.

(4) *Flow rule*:

The evolution equation for $\mathbf{F}^{\mathrm{p}}$ is

$$\dot{\mathbf{F}}^{\mathrm{p}} = \mathbf{D}^{\mathrm{p}}\mathbf{F}^{\mathrm{p}}, \quad \mathbf{F}^{\mathrm{p}}(\mathbf{X}, 0) = \mathbf{1}, \tag{2.8}$$

with $\mathbf{D}^{\mathrm{p}}$ given by the flow rule

$$\mathbf{D}^{\mathrm{p}} = v^{\mathrm{p}}\left(\frac{\mathbf{T}_0^{\mathrm{e}} - \mathbf{S}_{\mathrm{back}}}{2\bar{\tau}}\right), \qquad v^{\mathrm{p}} = v_0\left(\frac{\bar{\tau}}{s - \alpha\sigma}\right)^{\frac{1}{m}}, \quad 0 < m \leqslant 1, \tag{2.9}$$

where

$$\bar{\tau} = \frac{1}{\sqrt{2}}|\mathbf{T}_0^{\mathrm{e}} - \mathbf{S}_{\mathrm{back}}|, \quad \text{and} \quad v^{\mathrm{p}} = \sqrt{2}|\mathbf{D}_0^{P}|, \tag{2.10}$$

---

[5] Cf., Treloar (1975), Arruda and Boyce (1993) and Anand (1996).

[6] To evaluate $x = \mathscr{L}^{-1}(y)$ for a given y in the range $0 < y < 1$, we numerically solve the non-linear equation $f(x) = \mathscr{L}(x) - y = 0$ for x.

[7] Also see Arruda and Boyce (1993).

are an equivalent shear stress and equivalent plastic shear strain-rate, respectively. Here, ν_0 is a reference plastic shear strain-rate, α a pressure sensitivity parameter, and m a strain-rate sensitivity parameter. The limit $m \rightarrow 0$ renders (2.9) rate-independent, while $m = 1$ renders (2.9) linearly viscous.

(5) *Evolution equations for the internal variables s and η:*

The evolution of s and η is taken to be governed by the coupled differential equations [8]

$$\left.\begin{aligned} \dot{s} &= h_0\left(1-\tfrac{s}{\tilde{s}(\eta)}\right)\nu^{\mathrm{p}}, \quad s(\mathbf{X},0)=s_0, \\ \dot{\eta} &= g_0\left(\tfrac{s}{s_{\mathrm{cv}}}-1\right)\nu^{\mathrm{p}}, \quad \eta(\mathbf{X},0)=0, \end{aligned}\right\} \tag{2.11}$$

with

$$\tilde{s}(\eta) = s_{\mathrm{cv}}[1+b(\eta_{\mathrm{cv}}-\eta)], \tag{2.12}$$

where $\{h_0, g_0, s_0, s_{\mathrm{cv}}, b, \eta_{\mathrm{cv}}\}$ are additional material parameters. Here $\tilde{s} = \tilde{s}(\eta)$ is a saturation value of s: $\dot{s}$ is positive for $s < \tilde{s}$ and negative for $s > \tilde{s}$. By definition ν^{p} is non-negative. Assuming that $\nu^{\mathrm{p}} > 0$, all solutions to the pair of evolution equations satisfy

$$s \rightarrow s_{\mathrm{cv}} \quad \text{and} \quad \eta \rightarrow \eta_{\mathrm{cv}} \quad \text{as } t \rightarrow \infty.$$

We restrict attention to the initial conditions $s = s_0$ with

$$s_0 \leqslant s \leqslant s_{\mathrm{cv}}(1+b\eta_{\mathrm{cv}}).$$

Also, as is tacit from $(2.11)_2$, the free-volume is measured from the value $\eta = 0$ in the virgin state of the material, and thus η at any other time represents a change in the free-volume from the initial state.

2.1. Modification of the constitutive model for large elastic volume changes. Fracture criteria

As indicated previously, many experiments indicate that hydrostatic tension plays a key role in the nucleation of internal cracks. To accommodate this physical observation, we modify the elastic part of the constitutive model to allow for large elastic volume changes. Thus, instead of using the stress–strain pair

$$\mathbf{E}^{\mathrm{e}} = \frac{1}{2}(\mathbf{C}^{\mathrm{e}}-\mathbf{1}), \quad \mathbf{T}^{\mathrm{e}} = \mathbf{R}^{\mathrm{e}\mathrm{T}}\mathbf{T}\mathbf{R}^{\mathrm{e}},$$

which is appropriate for small elastic stretches, we shall use the conjugate stress–strain pair

$$\mathbf{E}^{\mathrm{e}} = \frac{1}{2}\ln\mathbf{C}^{\mathrm{e}}, \quad \mathbf{T}^{\mathrm{e}} = (\det\mathbf{F}^{\mathrm{e}})\mathbf{R}^{\mathrm{e}\mathrm{T}}\mathbf{T}\mathbf{R}^{\mathrm{e}}, \tag{2.13}$$

which is appropriate for large elastic stretches in isotropic materials (Anand, 1979) to formulate the elastic stress–strain relations. Then denoting the volumetric and deviatoric part of the logarithmic elastic strain $(2.13)_1$ by

$$\epsilon^{\mathrm{e}} = \operatorname{tr}\mathbf{E}^{\mathrm{e}}, \quad \mathbf{E}^{\mathrm{e}}_0 = \mathbf{E}^{\mathrm{e}} - \frac{1}{3}\epsilon^{\mathrm{e}}\mathbf{1}, \tag{2.14}$$

respectively, the elastic free energy is taken as [9]

---

[8] We expect that $\tilde{s}$ (and perhaps h_0 and g_0) may, in general, depend on ν^{p}, but currently there is insufficient experimental evidence to warrant such a refinement.

[9] The form for the volumetric response is motivated by the Universal Binding Energy Relation (UBER) introduced by Rose et al. (1983) in a one-dimensional context of separation between atomic planes in metals.

$$\psi^{\mathrm{e}} = G|\mathbf{E}_0^{\mathrm{e}}|^2 + \Big(K(\epsilon_{\mathrm{c}}^{\mathrm{e}})^2\Big)\left\{1 - \left(1 + \frac{\epsilon^{\mathrm{e}}}{\epsilon_{\mathrm{c}}^{\mathrm{e}}}\right)\exp\left(-\frac{\epsilon^{\mathrm{e}}}{\epsilon_{\mathrm{c}}^{\mathrm{e}}}\right)\right\}, \tag{2.15}$$

where G, K, and $\epsilon_{\mathrm{c}}^{\mathrm{e}}$ are the shear modulus, the ground state bulk modulus, and a critical value of the elastic volumetric strain, respectively.

The conjugate stress $(2.13)_2$ is then given by

$$\mathbf{T}^{\mathrm{e}} = \frac{\partial\psi^{\mathrm{e}}}{\partial\mathbf{E}^{\mathrm{e}}} = 2G\mathbf{E}_0^{\mathrm{e}} + \left\{K\exp\left(-\frac{\epsilon^{\mathrm{e}}}{\epsilon_{\mathrm{c}}^{\mathrm{e}}}\right)\right\}\epsilon^{\mathrm{e}}\mathbf{1}, \tag{2.16}$$

and in this case the mean normal stress $\sigma = (1/3)\,\mathrm{tr}\,\mathbf{T}^{\mathrm{e}}$ is

$$\sigma = \left\{K\exp\left(-\frac{\epsilon^{\mathrm{e}}}{\epsilon_{\mathrm{c}}^{\mathrm{e}}}\right)\right\}\epsilon^{\mathrm{e}}. \tag{2.17}$$

Hence, the generalized bulk modulus in this constitutive model is

$$\widetilde{K} = \frac{\partial\sigma}{\partial\epsilon^{\mathrm{e}}} = K\left\{1 - \frac{\epsilon^{\mathrm{e}}}{\epsilon_{\mathrm{c}}^{\mathrm{e}}}\right\}\exp\left\{\frac{\epsilon^{\mathrm{e}}}{\epsilon_{\mathrm{c}}^{\mathrm{e}}}\right\}, \quad \text{with} \quad \tilde{K} \to K, \quad \text{as } \epsilon^{\mathrm{e}} \to 0. \tag{2.18}$$

Eq. (2.17) for the mean normal stress σ may be rewritten as

$$\sigma = \sigma_{\mathrm{c}}\left(\frac{\epsilon^{\mathrm{e}}}{\epsilon_{\mathrm{c}}^{\mathrm{e}}}\right)\exp\left\{1 - \frac{\epsilon^{\mathrm{e}}}{\epsilon_{\mathrm{c}}^{\mathrm{e}}}\right\}, \quad \text{where } \sigma_{\mathrm{c}} \equiv \frac{K\epsilon_{\mathrm{c}}^{\mathrm{e}}}{e}, \tag{2.19}$$

and e is the Naperian/Euler number. A plot of $(\sigma/\sigma_{\mathrm{c}})$ versus $(\epsilon^{\mathrm{e}}/\epsilon_{\mathrm{c}}^{\mathrm{e}})$, Fig. 1, clearly shows that σ attains a maximum value σ_{c}, when $\epsilon^{\mathrm{e}} = \epsilon_{\mathrm{c}}^{\mathrm{e}}$. The quantity σ_{c} represents the *cavitation strength* of the material. Note that for most practical purposes the material loses any stress-carrying capacity when $\epsilon^{\mathrm{e}} \gtrapprox (4\text{to } 10) \times \epsilon_{\mathrm{c}}^{\mathrm{e}}$. Also note that the integral

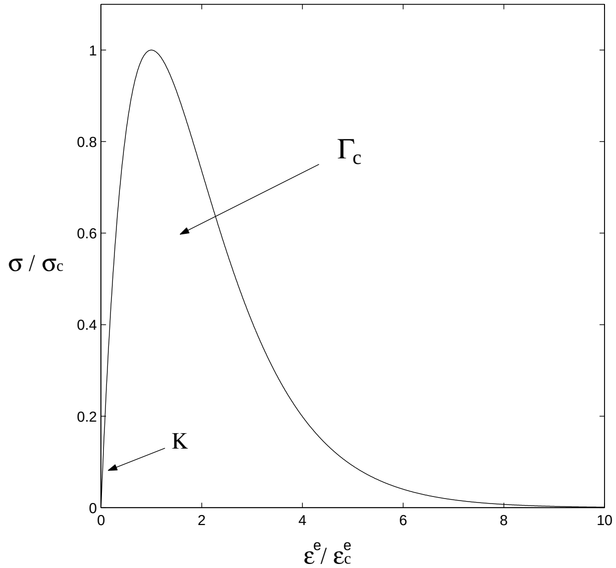

Fig. 1. Relationship between the mean normal stress and the elastic volumetric strain. The initial slope is the ground state bulk modulus K, and the cavitation fracture energy per unit volume is Γ_{c}.

$$\Gamma_{\mathrm{c}} = \int_0^{\infty} \sigma \, \mathrm{d}\epsilon^{\mathrm{e}} = e\sigma_{\mathrm{c}}\epsilon_{\mathrm{c}}^{\mathrm{e}} = K(\epsilon_{\mathrm{c}}^{\mathrm{e}})^2, \tag{2.20}$$

represents a *cavitation fracture energy* per unit volume of the relaxed configuration.

In order to model fracture in polycarbonate we introduce two simple local fracture criteria:

(1) Brittle fracture will be taken to occur when a local elastic volumetric strain ϵ^{e} reaches a failure value $\epsilon_{\mathrm{f}}^{\mathrm{e}}$:

$$\epsilon^{\mathrm{e}} \leqslant \epsilon_{\mathrm{f}}^{\mathrm{e}}. \tag{2.21}$$

(2) Ductile fracture will be taken to occur when the effective plastic stretch λ^{p} reaches a critical value $\lambda_{\mathrm{f}}^{\mathrm{p}}$:

$$\lambda^{\mathrm{p}} \leqslant \lambda_{\mathrm{f}}^{\mathrm{p}}. \tag{2.22}$$

We have implemented our constitutive model in the finite element computer program ABAQUS/Explicit ABAQUS (2002) by writing a user material subroutine. This finite element program permits the modelling of failure, when user-specified critical values of certain parameters are reached, by an element removal technique.

3. Experimental program to determine material parameters for polycarbonate

In this section we present the results of our efforts at estimation of the material parameters for our constitutive model, and also the failure values of the elastic volumetric strain and effective plastic stretch in the brittle and ductile fracture criteria. Recall that the material parameters that need to be determined are

(1) The elastic shear and bulk moduli (G, K) and the critical value of the elastic volumetric strain $\epsilon_{\mathrm{c}}^{\mathrm{e}}$ in the elastic part of the free energy.
(2) The parameters $(\mu_{\mathrm{R}}, \lambda_{\mathrm{L}})$ in the plastic part of the free energy.
(3) The parameters $\{\nu_0, m, \alpha, h_0, g_0, s_{\mathrm{cv}}, b, \eta_{\mathrm{cv}}, s_0\}$ in the flow rule and the evolution equations for (s, η).
(4) The parameters $(\epsilon_{\mathrm{f}}^{\mathrm{e}}, \lambda_{\mathrm{f}}^{\mathrm{p}})$ in the failure criteria.

The values of (G, K) are determined by measuring the Young's modulus and Poisson's ratio of the material in a compression experiment and using standard conversion relations of isotropic elasticity to obtain the elastic shear and bulk moduli. The parameters $\{\nu_0, m\}$ are estimated by conducting a strain-rate jump experiment in simple compression, and the pressure sensitivity parameter α is estimated from compression experiments under superposed hydrostatic pressure reported in the literature. The parameters $\{h_0, g_0, s_{\mathrm{cv}}, b, \eta_{\mathrm{cv}}, s_0\}$ and $(\mu_{\mathrm{R}}, \lambda_{\mathrm{L}})$ may be estimated by fitting a stress–strain curve in compression to large strains. The parameter $\lambda_{\mathrm{f}}^{\mathrm{p}}$ for ductile failure is obtained by fitting a load–displacement curve obtained from a specimen which has been extended to failure in tension. And finally, the value of $(\epsilon_{\mathrm{c}}^{\mathrm{e}}, \epsilon_{\mathrm{f}}^{\mathrm{e}})$ may be estimated from a load–displacement curve from a sharply notched-bar tension specimen extended to failure in tension.

A stress–strain curve for polycarbonate obtained from a monotonic simple compression experiment conducted at a constant logarithmic strain-rate of −0.001/s is shown in Fig. 2; absolute values of stress and strain are plotted. [10] After an initial approximately linear region, the stress–strain curve becomes markedly

---

[10] As is well known, the mechanical response of amorphous thermoplastics is very sensitive to prior thermomechanical processing history. The experiments reported in this paper were conducted on polycarbonate specimens which were annealed at the glass transition temperature of this material, 145 °C, for 2 h, and then furnace-cooled to room temperature in approximately 15 h. The experiments reported here were conducted under isothermal conditions at room temperature.

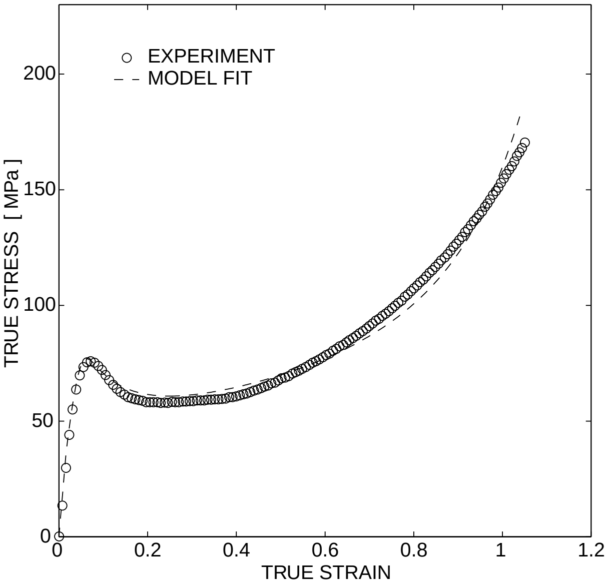

Fig. 2. Fit of the constitutive model to the stress–strain response of polycarbonate in simple compression.

non-linear prior to reaching a peak in the stress; the material then strain-softens to a quasi-plateau before beginning a broad region of rapid strain hardening. Using a value of $\alpha = 0.08$ from the data reported by Spitzig and Richmond (1979), a value of $v_0 = 0.0017\ \mathrm{s}^{-1}$ and a strain-rate-sensitivity parameter $m = 0.011$ obtained from a strain-rate jump experiment, the parameters $\{G, K, \mu_R, \lambda_L, h_0, g_0, s_{cv}, b, \eta_{cv}, s_0\}$ were estimated by fitting the stress–strain curve for polycarbonate in simple compression, Fig. 2. The fit was performed by judiciously adjusting the values of these parameters in finite element simulations of a simple compression experiment (assuming homogeneous deformation) using a single ABAQUS/C3D8R element. After a few attempts, a reasonable fit was obtained, and this is shown in Fig. 2. The list of parameters obtained using this heuristic calibration procedure are: [11]

$$G = 0.857\mathrm{GPa} \quad K = 2.24\ \mathrm{GPa} \quad \mu_R = 11.0\ \mathrm{MPa} \quad \lambda_L = 1.45 \quad v_0 = 0.0017\ \mathrm{s}^{-1} \quad m = 0.011$$
$$\alpha = 0.080 \quad s_0 = 20.0\ \mathrm{MPa} \quad s_{cv} = 24.0\ \mathrm{MPa} \quad h_0 = 2.75\ \mathrm{GPa} \quad b = 825 \quad g_0 = 6.0 \times 10^{-3}$$
$$\eta_{cv} = 0.001.$$

In order to estimate the value of the parameter λ_f^p for ductile failure, we conducted several tension experiments. The experiments were performed under displacement control at 0.0125 mm/s on specimens with a gauge section of initial diameter of 6.35 mm, and length of 25.4 mm. A representative experimentally-measured load–displacement response is shown in Fig. 3. At the peak load of about 2.3 kN, a pronounced neck forms in the gauge section, and the load subsequently decreases to an approximate plateau value of 1.6 kN. The neck then propagates along the gauge section until a displacement of 15.8 mm is reached. At the maximum displacement, the entire section over which the neck has propagated develops a profuse number of ring cracks around the circumference, and final separation occurs somewhere in the

---

[11] This list, although not unique, is adequate for present purposes.

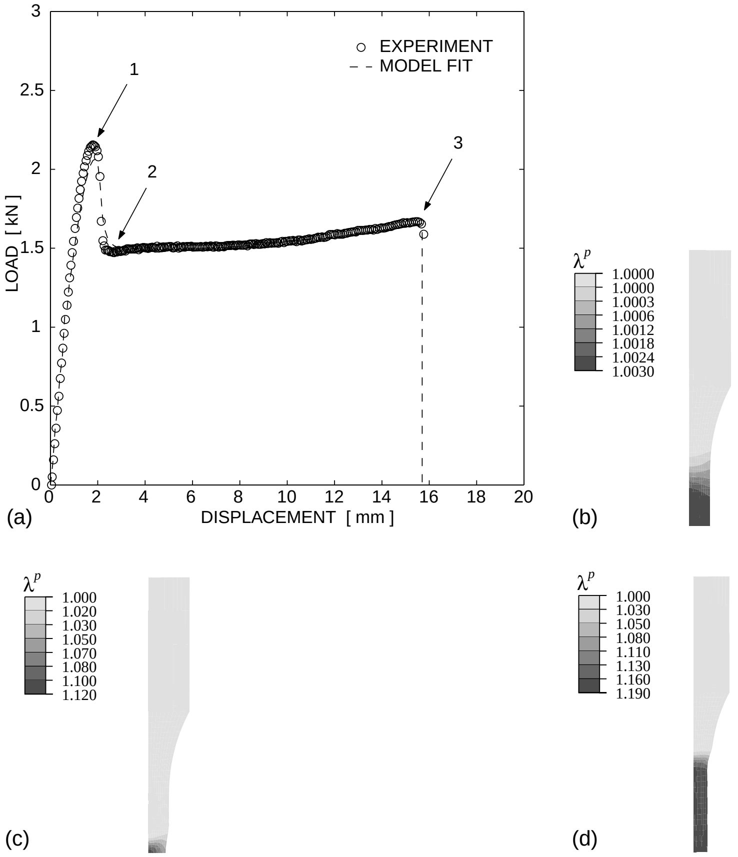

Fig. 3. Fit of the ductile failure criterion in simple tension: (a) experimental and numerical curves. Three displacement levels of interest are marked on the load displacement-curve. Contour plots of effective plastic stretch λ^{p} at (b) displacement level 1, (c) displacement level 2, and (d) displacement level 3.

necked region. To check the repeatability of the failure response, five identical specimens were tested; the measured displacements at fracture varied less than 5%.

To numerically model a tension experiment, one half of a specimen was meshed with 390 ABAQUS/CAX4R axi-symmetric elements. The constitutive parameters used in the simulation are those obtained from the fitting exercise for the compression experiments, and in this calibration step, the only adjustable parameter is the failure value of the effective plastic stretch, $\lambda_{\mathrm{f}}^{\mathrm{p}}$; this was adjusted to match the final displacements to "ductile" fracture. The fit shown in Fig. 3 is obtained with

$$\lambda_{\mathrm{f}}^{\mathrm{p}} = 1.192.$$

Note that prior to the final ductile fracture, the load–displacement response from the numerical simulation shown in Fig. 3 constitutes a prediction for this response. Contour plots of the effective plastic stretch λ^{p} are shown in Fig. 3b–d at the three displacement levels which have been marked by arrows in Fig. 3a. As can be seen from the contour plots, the deformation is homogeneous until the peak load, location 1, is attained at a maximum value of λ^{p} of 1.003. Subsequent to the peak load, a localized neck forms at the center of the gauge section, location 2, and here the maximum value of λ^{p} reaches 1.120. As the neck

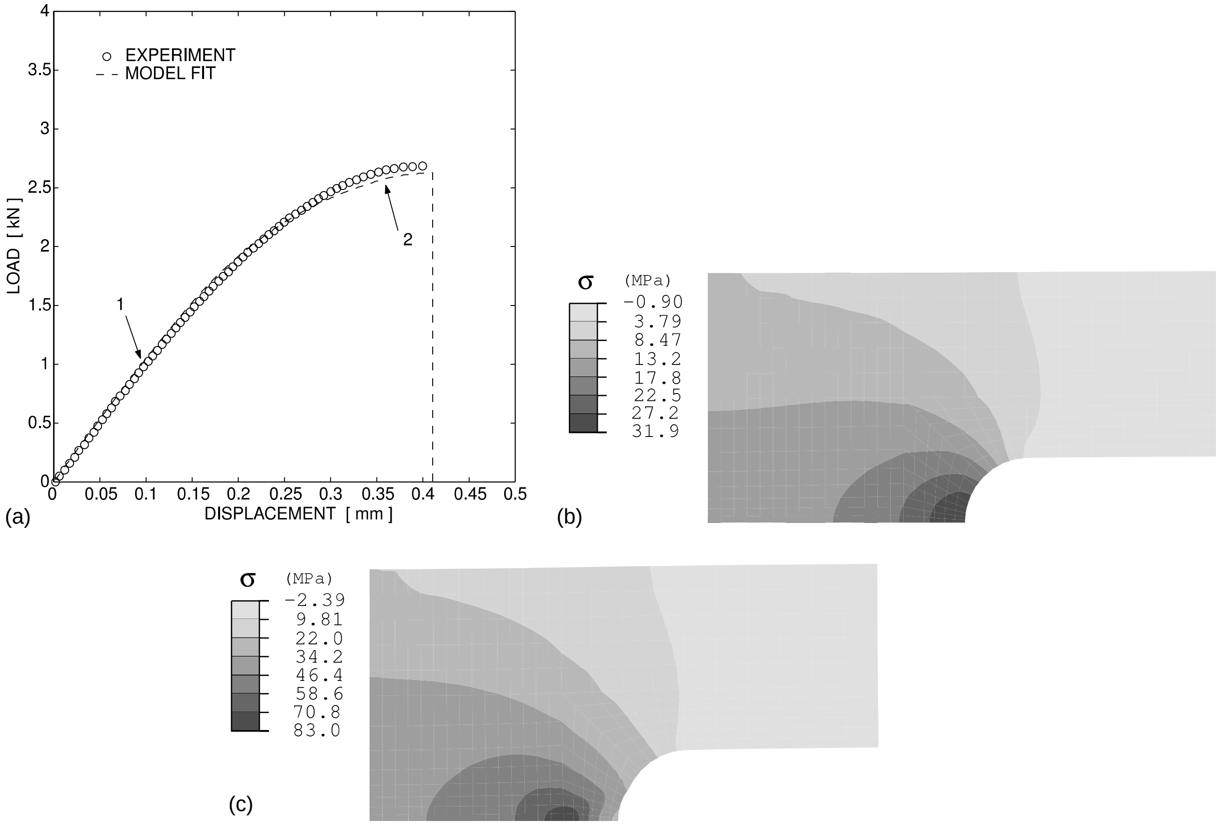

Fig. 4. (a) Fit of the brittle failure criterion in tension of a notched-bar specimen. Two displacement levels are marked on the load–displacement curve. Contour plots of mean normal stress σ at (b) location 1, and (c) location 2. The axis of the notched cylinder corresponds to the left edge of the figures in (b) and (c).

propagates along the gauge section, λ^{p} continues to increase until it reaches a maximum value of 1.192, at location 3, at which stage ductile fracture occurs.

To complete the calibration procedure one needs to determine the remaining parameters $(\epsilon_{\mathrm{c}}^{\mathrm{e}}, \epsilon_{\mathrm{f}}^{\mathrm{e}})$. To do this, notched-bar tension experiments were conducted. In such experiments a state of high mean normal stress is generated ahead of the notch, and brittle fracture is expected to occur if the notch is sufficiently sharp. The specimen geometry chosen to achieve this goal is a 12.7 mm cylindrical bar with a notch of 3.18 mm depth and 1.80 mm width; the radius at the notch root is 0.90 mm. An extensometer was used to measure the local relative displacement across the notch as the specimen was extended at a rate of 0.0125 mm/s. A representative experimentally-measured load–displacement response curve is shown in Fig. 4. The specimen fails abruptly at a displacement of about 0.4 mm. The fracture surfaces show a smooth region with an rms roughness of 43 nm ahead of the notch root, indicative of a “brittle” mechanism of failure, together with an indication of a more ductile failure response at the notch root. In order to check the repeatability of the fracture response, five specimens were tested and the measured displacements at fracture were found to vary by less than 4%.

To numerically model a notched-bar tension experiment, one half of the specimen was meshed with 390 ABAQUS/CAX4R axi-symmetric elements. We note that in this calibration step, the only adjustable parameters are $(\epsilon_{\mathrm{c}}^{\mathrm{e}}, \epsilon_{\mathrm{f}}^{\mathrm{e}})$. Since, $\epsilon_{\mathrm{c}}^{\mathrm{e}} = (\sigma_{\mathrm{c}} e)/K$, and the value of $K = 2.24$ GPa has been fixed, we adjust the value of σ_c and the ratio $\chi_f = \epsilon_f^e/\epsilon_c^e$, to fit the experimental load–displacement curve. The quality of the fit with the values [12] of

$$\sigma_c = 83.5 \text{ MPa} \quad \text{and} \quad \chi_f = 4.0,$$

is shown in Fig. 4a. These values for (σ_c, χ_f) correspond to

$$\epsilon_c^e = 0.1013, \quad \text{and} \quad \epsilon_f^e = 0.4053.$$

Also shown in Fig. 4b and c are contour plots of the mean normal stress σ at two different displacement levels indicated by arrows in Fig. 4a. During the initial linear loading stage, σ is maximum at the root of the notch, as can be observed in Fig. 4b. As deformation progresses, the load–displacement response becomes non-linear, a plastic zone develops at the notch root, and the maximum value of σ becomes concentrated ahead of the zone of plastic deformation. Brittle fracture eventually initiates in the region of high triaxiality, and the crack propagates across the specimen. This response is consistent with the experimentally-observed mostly "brittle" fracture surface.

The parameters obtained from these three calibration steps complete the material parameter determination for polycarbonate. In the next section we use the calibrated model to compare numerical predictions for both the deformation and failure response in four-point bending of a "blunt"-notched specimen geometry and a "sharp"-notched specimen geometry against corresponding physical experiments.

4. Ductile and brittle failure in notched-bend experiments

Four-point bending experiments were conducted on the specimen geometries shown in Fig. 5. As indicated in this figure, specimens with a blunt notch of a root radius of 4.76 mm and specimens with a sharp notch of a root radius of 1.98 mm radius were tested. A specimen width of 50 mm was chosen so as to approximate plane strain conditions at the notch root. A four-point bending fixture was utilized with the specimen centerline coincident with the centerline of the fixture. The experiments were performed by displacing the center rollers relative to the outer rollers at a constant displacement rate of 2 mm/min. All rollers were constrained during the experiments to ensure that they did not rotate.

4.1. Bending of the blunt-notched beam

The load–displacement response for the blunt-notched specimen is shown in Fig. 6a. Three displacement levels of interest are marked on the load–displacement curve. Fig. 6b–d show three micrographs, corresponding to the indicated displacement levels, of the specimen cross-section ahead of the notch. The micrographs were taken in the unloaded configuration from polished cross-sections of the specimen. The image taken at location 1 shows that a zone of plastic deformation (by the shear-yielding mechanism) has developed at the notch root. At location 2, the plastic zone has extended a significant distance through the thickness of the specimen, and plastic-deformation is also seen to have occurred at the back-face of the specimen. The abrupt drop in the load–displacement curve indicates the initiation of failure; this event is due to the nucleation of a crack at the notch root, and once the crack nucleates, it propagates in a stable

---

[12] Note that this value of σ_c for polycarbonate is very similar to the value previously estimated by Narisawa and his colleagues, e.g. Narisawa and Yee (1993).

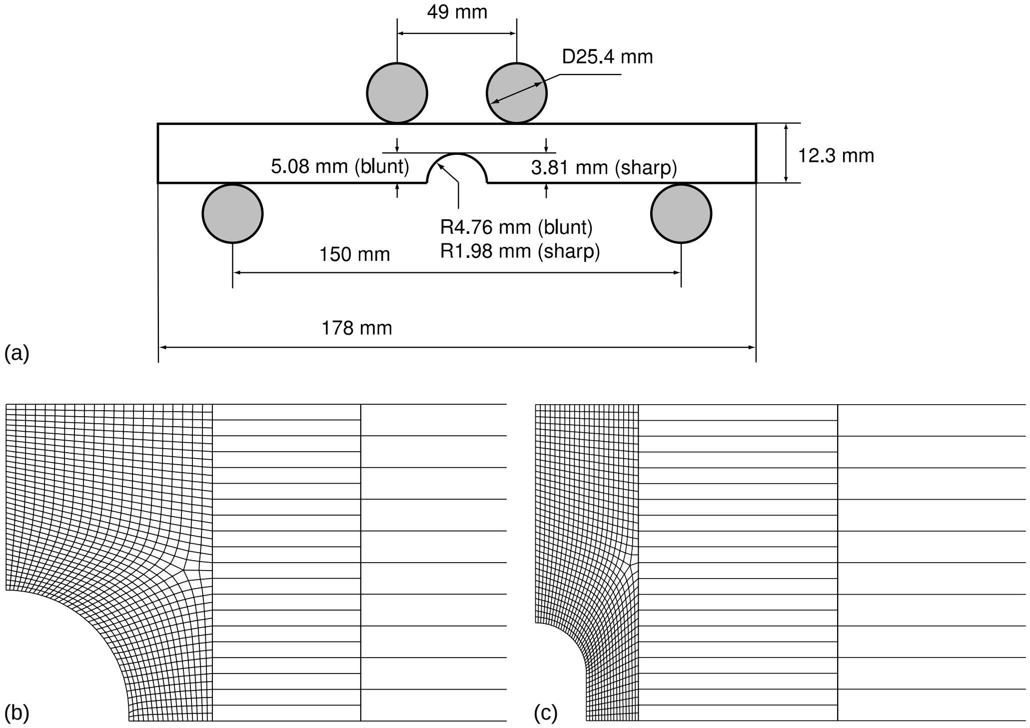

Fig. 5. (a) Geometry of four-point bending experiments. All specimens have a 50 mm nominal width. (b) Detail of finite element mesh at the notch root used to model the blunt-notched specimen. (c) Detail of finite element mesh at the notch root used to model the sharp-notched specimen.

manner through the thickness of the specimen. The crack is clearly visible in the micrograph corresponding to location 3. Thus, for the case of the blunt-notched specimen in bending, the macroscopic observation is that the structure fails in a ductile manner as evidenced by the attainment of large plastic stretches prior to crack initiation, and after initiation the crack propagates in a stable manner until final fracture.

To simulate bending of the blunt-notched beam, one-half of the beam is modelled using 1509 ABAQUS/CPE4R plane strain elements with reduced integration. A detail of the finite element mesh at the notch root is shown in Fig. 5. The load–displacement curve from the numerical simulation is compared against the experimental response in Fig. 7. While not perfect, the overall characteristics of the load–displacement curve and final failure are reasonably well predicted by the constitutive model and the ductile fracture criterion.

Four displacement levels of interest are marked on the numerical load–displacement curve shown in Fig. 7. In Fig. 8 we show contour plots of the effective plastic stretch λ^{p} corresponding to these displacement levels:

- At location 1, Fig. 8a, just prior to the initial peak on the load–displacement curve, a small plastic zone has developed around the notch root, and λ^{p} has a maximum value at the notch root of 1.014. This is physically similar to the plastic zone seen in Fig. 6b at an approximately similar location on the load–displacement curve of the physical experiment.

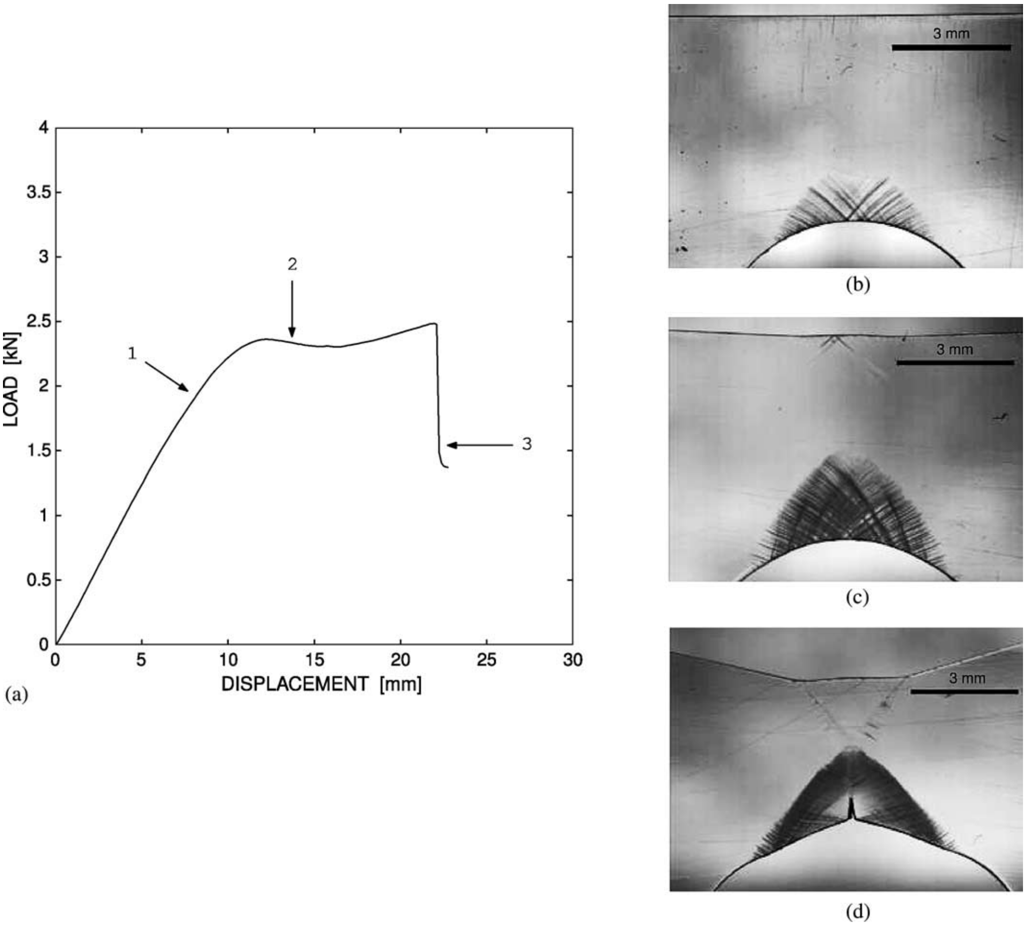

Fig. 6. Four-point bending of a blunt-notched polycarbonate specimen: (a) Load–displacement curve. Micrographs of unloaded specimen cross-sections are shown at: (b) location 1, (c) location 2, and (d) location 3 as indicated on the load–displacement curve.

- At location 2, Fig. 8b, the plastic zone at the notch root has grown in size, with a maximum value of $\lambda^{\mathrm{p}} = 1.110$ at a position slightly offset from the notch root; the back-face has deformed plastically. These features are physically similar to the plastic zone seen in Fig. 6c at an approximately similar location on the load–displacement curve of the physical experiment.
- At location 3, Fig. 8c, the plastic zone at the notch root has grown further in size. The effective plastic stretch has reached a maximum value of 1.192, which is equal to the failure value of $\lambda^{\mathrm{p}}_{\mathrm{f}}$, and ductile failure is seen to initiate at an element slightly offset from the centerline notch root. Recall that we are modelling failure by the element removal technique.
- By location 4, Fig. 8d, additional elements have reached the ductile fracture condition $\lambda^{\mathrm{p}} = \lambda^{\mathrm{p}}_{\mathrm{f}}$, and the corresponding elements have been removed. As the ductile failure process progresses from location 3 to location 4, the "crack" propagates both towards the specimen centerline and into the beam, as indicated in Fig. 8d. These features of ductile fracture are physically similar to those seen in Fig. 6d at an approximately similar location on the load–displacement curve of the physical experiment.

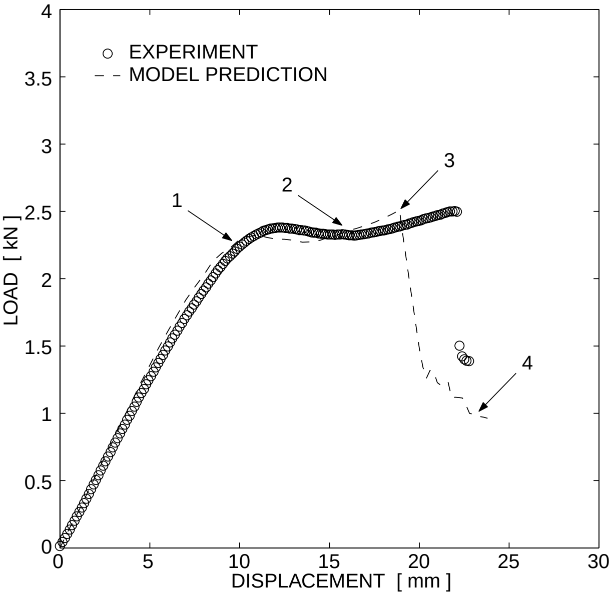

Fig. 7. Comparison of the prediction of the load–displacement response for blunt-notched beam bending against the experiment.

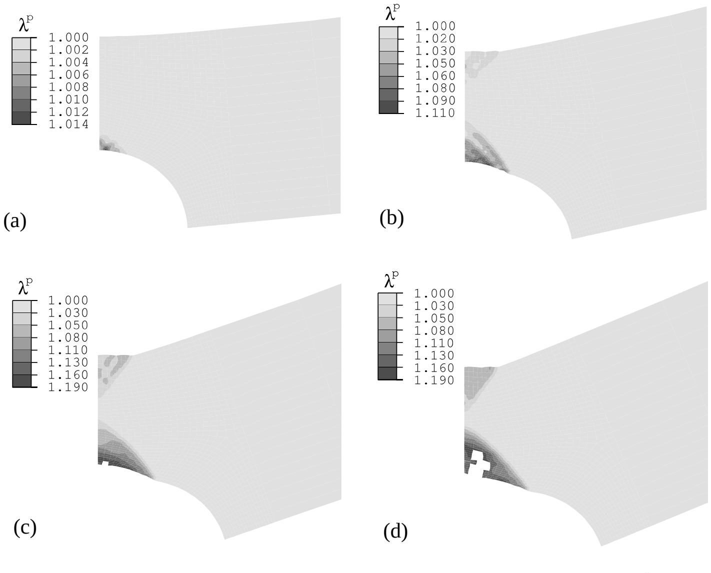

Fig. 8. Prediction of the fracture process in blunt-notched beam bending. Contour plots of λ^p corresponding to (a) location 1, (b) location 2, (c) location 3, and (d) location 4 as indicated on the predicted curve in Fig. 7. Ductile failure initiates at the notch root as indicated in (c) and propagates into the beam as seen in (d).

4.2. Bending of the sharp-notched beam

Fig. 9a shows the load–displacement response when the sharp-notched beam is subjected to bending under the same loading conditions as were used for the blunt-notched beam. The initial load–displacement

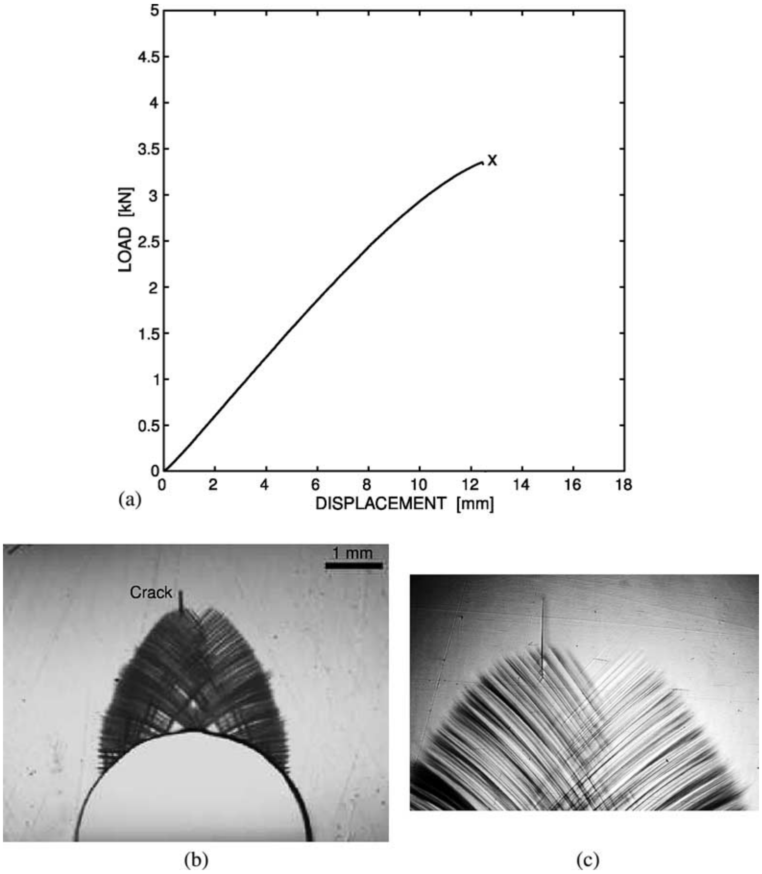

Fig. 9. Four-point bending of a sharp-notched polycarbonate specimen: (a) load–displacement curve with "x" indicating fracture. (b) Micrograph of unloaded specimen cross-section at incipient fracture. The crack initiates at the apex of the plastic zone. (c) Close-up of the crack at the apex of the plastic zone.

response of the sharp-notched specimen is similar to that of the blunt-notched experiment; here, however, the material fails abruptly at a displacement of 12.4 mm. An investigation of the fracture surface where the crack initiates reveals a surface roughness which varies in the nanometer range; [13] this indicates a fracture initiation mechanism which is "brittle" in nature. A separate experiment was conducted and stopped just prior to the point of fracture. An image of the polished cross-section is shown in Fig. 9b. Note that in addition to the shear-yielding plastic zone, one clearly sees a crack-like feature at the tip of the plastic zone. [14] For more exhaustive experimental observations of such features in sharp-notched beams, see Ishikawa et al. (1977) and Zuber (1985). The fracture surface of the beam shows a smooth surface ahead of the notch root and into the cross-section, indicative of brittle fracture, and also a small ligament at the notch root which appears to have failed in a ductile manner.

To simulate bending of the sharp-notched beam bending, one-half of the beam is modelled using 1370 ABAQUS/CPE4R plane strain elements with reduced integration. A detail of the finite element mesh at the

---

[13] The measured rms surface roughness is 43 nm.

[14] Minor experimental misalignment may have offset the crack slightly from the loading centerline.

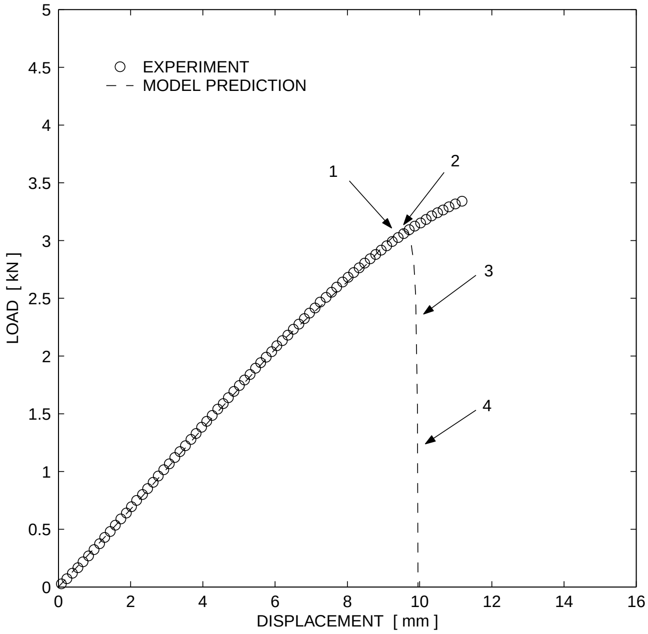

Fig. 10. Comparison of the predicted load–displacement response for the sharp-notched beam in bending against the experiment.

notch root is shown in Fig. 5. The load–displacement curve from the numerical simulation is compared against the experimental response in Fig. 10. Four displacement levels of interest are marked on the numerical load–displacement curve shown in Fig. 10. In Figs. 11 and 12 we show contour plots of the mean normal stress σ, and the effective plastic stretch λ^p corresponding to these displacement levels:

- At location 1, Figs. 11a and 12a, the maximum value of $\sigma = 82.1$ MPa occurs at a location just ahead of the notch root, while λ^p has a low value of only 1.100 at a location slightly offset from the notch root. Since the cavitation strength is $\sigma_c = 83.5$ MPa, location 1 is at a state of incipient brittle fracture.
- At location 2, Figs. 11b and 12b, we observe that brittle fracture has initiated at a location ahead of the plastic zone at the notch root. Comparison of the location of brittle fracture initiation with the micrograph in Fig. 9b indicates that the model accurately predicts the initiation site of brittle fracture.
- By location 3, Figs. 11c and 12c, the "crack" has extended deeper through the thickness of the specimen, but by now the remaining ligament between the crack and the free-surface of the notch has also been sufficiently plastically stretched to initiate ductile fracture at the free surface of the notch root.
- By location 4, Figs. 11d and 12d, the remaining ligament has failed completely by the ductile mechanism, and the crack has propagated further in a brittle fashion through the thickness of the beam. During this stage of the process, the values of λ^p remain below the critical value, as indicated in Fig. 12d.

Thus, in the sharp-notched beam the failure initiates due to the brittle fracture condition being met ahead of the plastic zone at the notch root, and the subsequent propagation of such a crack occurs by a competition between the brittle and ductile criteria being satisfied at different locations along the crack, depending on the local nature of the triaxiality constraints along the crack fronts. The constitutive model and fracture criteria nicely capture the intricate interplay of both the brittle fracture and ductile failure mechanisms, and provide a reasonable prediction of the load–displacement response of the sharp-notched beam in four-point bending.

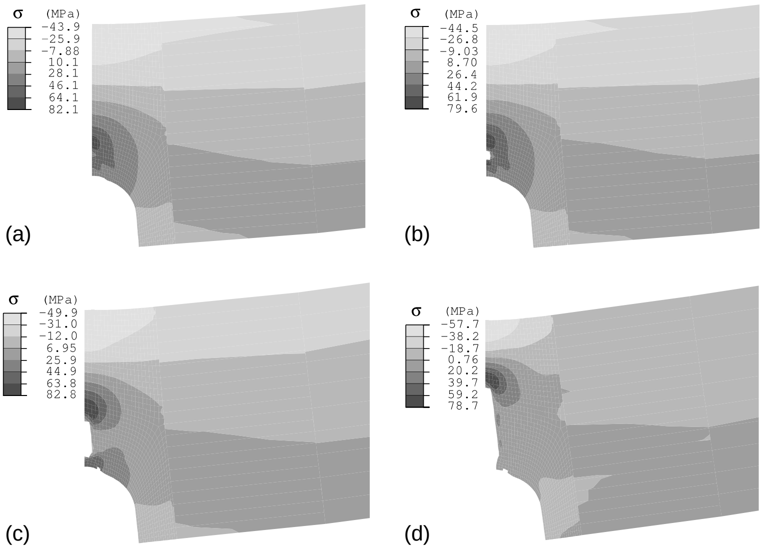

Fig. 11. Prediction of the fracture process in sharp-notch beam bending. Contour plots of σ corresponding to (a) location 1, (b) location 2, (c) location 3, and (d) location 4, as indicated on the predicted curve in Fig. 10. Brittle fracture initiates ahead of the notch root as indicated in (b).

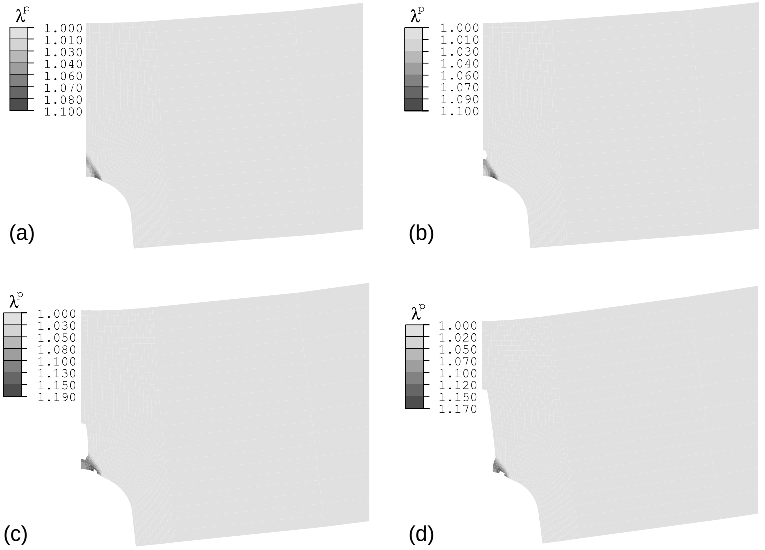

Fig. 12. Prediction of the fracture process in sharp-notched beam bending. Contour plots of λ^p corresponding to (a) location 1, (b) location 2, (c) location 3, and (d) location 4 as indicated on the predicted curve in Fig. 10. Ductile failure initiates at the notch root as indicated in (c) after brittle fracture initiates ahead of the notch.

5. Concluding remarks

We have developed a constitutive model and fracture criteria which can capture the competition between the ductile mechanism of inelastic deformation by shear-yielding and eventual ductile tearing, typically observed in amorphous thermoplastic materials under states of low triaxial tension, and the "cracking" phenomenon that is observed in states of high triaxial tension. Our constitutive model builds upon the recent theory of Anand and Gurtin (2004) for plastic deformation of amorphous polymeric materials. Our extensions consist of (a) generalizing the theory to allow for large elastic volume changes; (b) introducing a brittle fracture criterion based on the local elastic volumetric strain reaching a critical value; and (c) introducing a ductile fracture criterion based on an effective plastic stretch reaching a critical value. We have shown that the constitutive model and failure criteria, when suitably calibrated, are able to *quantitatively* predict the ductile failure response of blunt-notched beams of polycarbonate in bending, as well as the competition between the ductile and brittle mechanisms in more sharply-notched beams.

We recognize that, as with all finite element calculations, our numerical modelling of the ductile and brittle fracture processes may be "mesh-sensitive", and much needs to be done to refine the mesh (amongst other considerations) to be able to better represent such fracture processes. [15] However, as a first attempt to model such highly non-linear fracture processes in polymers, we consider that the proposed constitutive model and failure criteria adequately capture the competition between the ductile and brittle mechanisms of fracture initiation and propagation.

The present research needs to be extended by conducting more detailed experiments at various temperatures and strain-rates to see if the failure criteria continue to have predictive capabilities under different temperature and strain-rate conditions, [16] and by conducting experiments on specimen geometries that might exhibit an even more complicated interplay between the ductile and brittle fracture mechanisms. In addition, statistical aspects of fracture criteria also need to be elucidated.

Acknowledgements

Partial financial support for Brian P. Gearing was provided by the DuPont-MIT Alliance. We gratefully acknowledge the help of Cheng Su and Ting Zhu for initial contributions to the experiments and numerical simulations. The ABAQUS finite element code was made available under an academic license to MIT from HKS, Inc., Pawtucket, RI.

References

ABAQUS, 2002. Reference manuals, Hibbit, Karlsson & Sorenson Inc., Pawtucket, RI.

Anand, L., 1979. On H. Hencky's approximate strain-energy function for moderate deformations. ASME Journal of Applied Mechanics 46, 78–82.

Anand, L., 1996. A constitutive model for compressible elastomeric solids. Computational Mechanics 18, 339–352.

Anand, L., Gurtin, M.E., 2003. A theory of amorphous solids undergoing large deformations, with applications to polymers and metallic glasses. International Journal of Solids and Structures 40, 1465–1487.

Arruda, E.M., Boyce, M.C., 1993. Evolution of plastic anisotropy in amorphous polymers during finite straining. International Journal of Plasticity 9, 697–720.

Boyce, M.C., Parks, D.M., Argon, A.S., 1988. Large inelastic deformation of glassy polymers. Part 1: Rate dependent constitutive model. Mechanics of Materials 7, 15–33.

---

[15] We have not conducted an exhaustive "mesh-sensitivity" analysis for our numerical results.

[16] The experiments of Narisawa and his colleagues (as summarized in Narisawa and Yee, 1993) indicate that the value of σ_c for polycarbonate is approximately independent of strain-rate over a range of rates varying from 10^{-4} to 10^{-1} per second. However, given the strong dependence of the elastic moduli on temperature, we expect that the value of σ_c will decrease with increasing temperature. Thus, any adiabatic heating effects at higher strain-rates are also expected to lower the value of σ_c.

Ishikawa, M., Narisawa, I., Ogawa, H., 1977. Criterion for craze nucleation in polycarbonate. Journal of Polymer Science 15, 1791–1804.

Kroner, E., 1960. Allgemeine kontinuumstheorie der versetzungen und eigenspannungen. Archive for Rational Mechanics and Analysis 4, 273–334.

Lee, E.H., 1969. Elastic plastic deformation at finite strain. ASME Journal of Applied Mechanics 36, 1–6.

Narisawa, I., Yee, A.F., 1993. Crazing and fracture of polymers. Materials Science and Technology. A Comprehensive Treatment 12, 699–765.

Nimmer, R.P., Woods, J.T., 1992. An investigation of brittle failure in ductile notch-sensitive thermoplastics. Polymer Engineering and Science 32, 1126–1137.

Parks, D.M., Argon, A.S., Bagepalli, B., 1985. Large elastic-plastic deformation of glassy polymers. Part 1: Constitutive modeling, MIT, Program in Polymer Science and Technology Report.

Rose, J.H., Smith, J.R., Ferrante, J., 1983. Universal features of bonding in metals. Physical Review B 28, 1835–1845.

Spitzig, W.A., Richmond, O., 1979. Effect of hydrostatic pressure on the deformation behavior of polyethylene and polycarbonate in tension and compression. Polymer Engineering and Science 19, 1129–1139.

Treloar, L.R.G., 1975. The Physics of Rubber Elasticity, Oxford.

Wu, P.D., Van der Giessen, E., 1993. On improved network models for rubber elasticity and their applications to orientation hardening of glassy polymers. Journal of the Mechanics and Physics of Solids 41, 427–456.

Zuber, P.J., 1985. Initiation of ductile fracture from shear bands in *u*-notched four point bend tests, S.M. Thesis, Massachusetts Institute of Technology.